Mathematical Biosciences and Engineering

Research article

Impact of coronary bifurcated vessels flow-diameter scaling laws on fractional flow reserve based on computed tomography images (FFRCT)

Na Li[1], Bao Li[1], Yili Feng[1], Junling Ma[1], Liyuan Zhang[1], Jian Liu[2] and Youjun Liu[1,*]

[1] College of Life Science and Chemistry, Faculty of Environment and Life, Beijing University of Technology, Beijing, China

[2] Peking University People's Hospital, Beijing, China

* **Correspondence:** Email: lyjlma@ bjut.edu.cn; Tel: +861067396657; Fax: +861067396657.

Abstract: *Objective:* To explore the influence of the blood flow-diameter scaling laws of $Q\alpha D^3$, $Q\alpha D^{2.7}$ and $Q\alpha D^{7/3}$ on the numerical simulation of fraction flow reserve based on CTA images and to find the optimal exponents. *Methods:* 1) 26 patients with coronary artery disease were screened according to the inclusion criteria; 2) Microcirculation resistance (R_m) was calculated under the 3, 2.7 and 7/3 power of the flow-diameter scaling law, which were recorded as $3R_m$, $2.7R_m$ and $7/3R_m$, respectively; 3) $3R_m$, $2.7R_m$ and $7/3R_m$ were used as exit boundary conditions to simulate FFRCT, quoted as 3FFRCT, 2.7FFRCT and 7/3FFRCT, respectively; 4) The correlation and diagnostic performance between three kinds of FFRCT and FFR were analyzed. *Results:* The p-values of comparing 3Rm, 2.7Rm and 7/3Rm with FFR were 0.004, 0.005 and 0.010, respectively; the r value between 7/3FFRCT and FFR (0.96) was better than that of 3FFRCT (0.95) and 2.7FFRCT (0.95); the 95% LoA between 7/3FFRCT and FFR (-0.08~0.11) was smaller than that of 3FFRCT (-0.10~0.12) and 2.7FFRCT (-0.09~0.11); the AUC and accuracy of 7/3FFRCT [0.962 (0.805–0.999), 96.15%] were the same as those of 2.7FFRCT [0.962 (0.805–0.999), 96.15%] and better than those of 3FFRCT [0.944 (0.777–0.996), 92.3%]. The prediction threshold of 7/3FFRCT (0.791) was closer to 0.8 than that of 3FFRCT (0.816) and 2.7FFRCT (0.787). *Conclusion:* The blood flow-diameter scaling law affects the FFRCT simulation by influencing the exit boundary condition R_m of the calculation. With $Q\alpha D^{7/3}$, FFRCT had the highest diagnostic performance. The blood flow-diameter scaling law provides theoretical support for the blood flow distribution in the bifurcated vessel and improves the FFRCT model.

Keywords: blood flow-diameter scaling law; FFRCT; 0D/3D geometric multi-scale model;

microcirculation resistance; numerical calculation

1. Introduction

The coronary fraction flow reserve (FFR) represents the gold standard for the evaluation of myocardial ischemia [1–4]. However, it is measured through an invasive operation with adenosine injection; this represents a limitation in some patients who are intolerant to adenosine [3,5]. The rapid advancements in computational fluid dynamics and medical images made it possible to perform a personalized hemodynamic simulation based on medical images. By combining the advantages of computed tomography imaging (CTA) and FFR, a new non-invasive technique (FFRCT) was proposed to assess the coronary artery stenosis from both anatomical and functional aspects [6–9]. The consistency of FFRCT and FFR was evaluated in the multi-center, early prospective study of DISCOVER-FLOW (Diagnosis of Ischemia-Causing Stenoses Obtained Via Noninvasive Fractional Flow Reserve) [7,10,11]. The results showed a good consistency.

Taylor et al. laid the foundation for the numerical calculation of FFRCT in HeartFlow NXT [4, 9–13]. Calculating FFR based on the coronary CTA image includes five basic processes: 1) Based on the CTA images, the patient's accurate and personalized anatomical model of the epicardial coronary artery is constructed; 2) Based on the assumption that there is no vascular stenosis, the total coronary flow and the flow of each branch in the resting state are accurately evaluated; 3) Coronary microcirculation resistance is calculated at rest; 4) The change in the coronary microcirculation resistance is quantified under maximum hyperemia; 5) The control equation (N-S equation) of the coronary fluid is numerically calculated to obtain the flow rate and pressure in the coronary artery in the resting and hyperemic states, and FFR is calculated. Combining anatomy, physiology and computational fluid dynamics makes it possible to calculate the blood flow and pressure in the coronary arteries in a hyperemic state. However, in the second step, the coronary artery branch flow cannot be measured in the clinic, so the subsequent calculations cannot be performed. To solve this problem, the most commonly used method is based on the assumption of the blood flow diameter scaling law to evaluate the flow in bifurcated vessels.

The power-law scaling relationship has been assumed to be ubiquitous in biology and it is relevant to the domains of medicine, nutrition and ecology [14–16]. Eighty years ago, Murray proposed a compromise between the frictional and metabolic cost, expressed as a cost function. Murray's law predicts a universal exponent that is invariant (3.0) for all vascular trees with internal flows obeying laminar conditions [15,17,18]. Unlike Murray's law, Zhou et al. showed that the exponent of the blood-diameter scaling law is not necessarily equal to 3.0, but it depends on the ratio of the metabolic to viscous power dissipation of the tree of interest [19,20]. Subsequently, Lucian et al. proposed several power coefficient values (ranging from 2.1 to 3) based on the assumption that blood flow requires minimal energy, and they verified their suggestions with a bifurcated asymmetric vascular tree [21]. Eventually, 2.7 was extrapolated as the best exponent of the blood-diameter scaling law. Besides, Yunlong Huo et al. did not reference empirical parameters when constructing the coronary artery tree. They derived that the blood flow of the bifurcated vessel is proportional to the 7/3 power of the diameter based on the relationship between the predicted volume and diameter of the intraspecies scaling theory index 3.0 [17,22,23]. The above-mentioned widely used blood flow-diameter scaling laws are obtained by performing least-squares fitting of various organs

through a variety of animal experiments. However, for many blood flow diameter scaling laws, which one is suitable for the blood flow distribution of human coronary bifurcation vessels and how to perform the numerical calculation of FFRCT [24–26].

This study retrospectively calculated the microcirculation resistance under different blood flow-diameter scaling laws of 3, 2.7 and 7/3 and used it as the exit boundary condition of FFRCT in the simulation calculation. The accuracy of FFRCT was evaluated with invasive FFR as the standard, which derived the optimal blood flow-diameter scaling law that is suitable for the FFRCT simulation calculation. This provides a theoretical basis for the blood flow distribution of coronary bifurcation vessels and is significant for modifying the 0D/3D coupling model to improve the accuracy of FFRCT.

2. Materials and methods

In this study, an open-loop 0D/3D geometric multi-scale model was used to numerically simulate FFRCT under different blood flow diameter scaling laws. The accuracy of the simulation results of the three methods was evaluated with the clinically measured FFR as the evaluation standard. The whole research process included four main parts: the collection of physiological parameters and structural parameters, Rm calculation, the 0D/3D multi-scale model setting and comparative analysis of the simulation results, as shown in Figure 1.
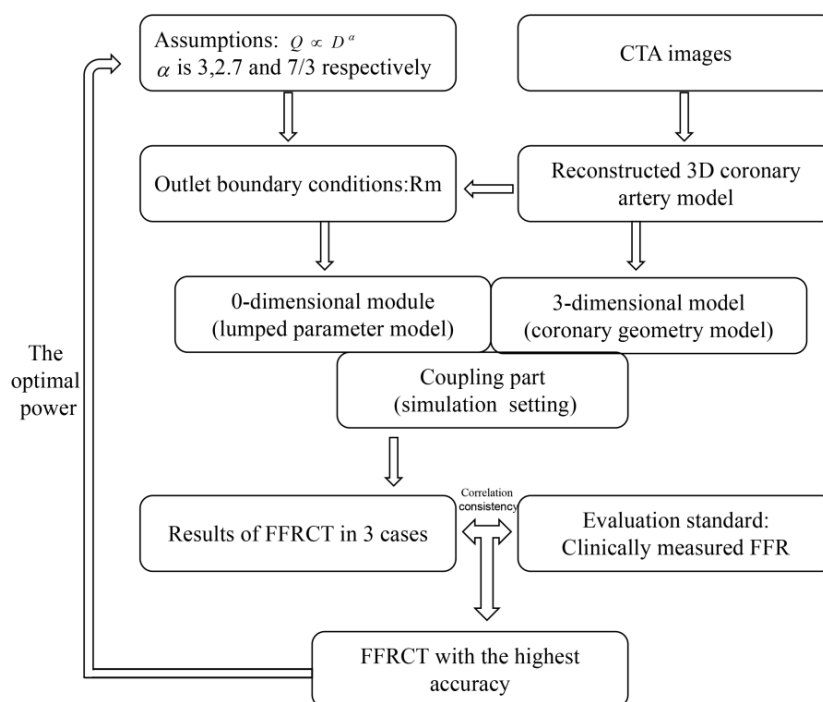

Figure 1. Flow chart of the research framework.

2.1. Study population and design

This study was designed as a retrospective study and approved by the ethics committee of Peking University People's Hospital. The coronary artery disease (CAD) patients enrolled in the

group signed an informed consent form.

The entire enrollment and exclusion process is shown in Figure 2. In detail, the inclusion and exclusion criteria of 50 stable and unstable CAD patients should meet the diagnostic criteria of local CAD patients. 9 patients were excluded due to clinical instability, 1 patient had arrhythmia, 3 patients had poor CT image quality resulting in incomplete reconstruction of the coronary artery tree, 7 patients were excluded due to stenosis before the first bifurcation node (the stenosis of 5 patients was located in the left main stem, while the stenosis of 2 patients was located in the proximal right coronary segment), 2 patients were excluded due to incomplete ultrasound results, 2 patients were excluded due to diabetes with suspected microcirculation dysfunction. Finally, 26 patients were enrolled in the group. Among which 19 patients had non-myocardial ischemia and 7 patients had myocardial ischemia.
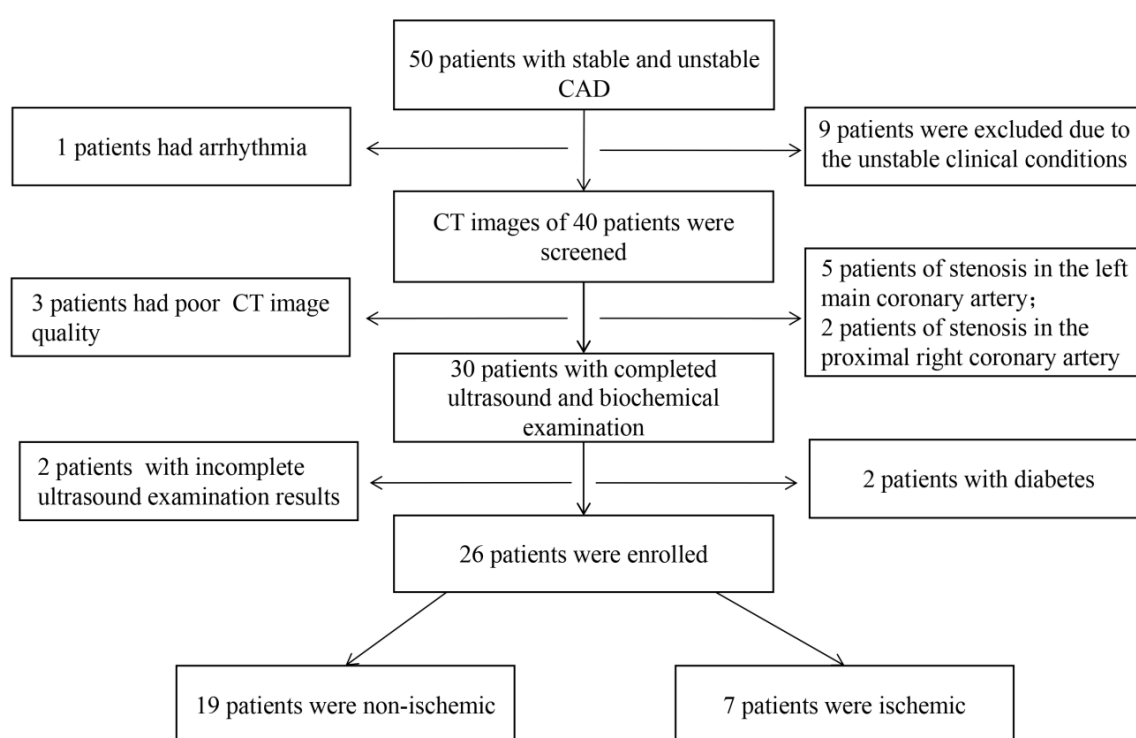

Figure 2. Enrollment and exclusion process of the study population.

Before invasive FFR measurement, multiple clinical examinations were required, such as brachial artery blood pressure measurement, CTA examination, ultrasound examination and biochemical examination. The FFR value was obtained in standard operating procedures. The patients were all in the supine position, and under the digital subtraction angiography machine (DSA, PHILIPS, Netherlands), adenosine triphosphate was injected at a uniform rate of $140\sim180\ \mu$ g/kg/min to make the coronary blood vessels reach the maximum hyperemia state. The interval between various inspections should not exceed 30 days.

2.2. Rm calculation under three kinds of flow-diameter scaling laws

The necessary information for the calculation of R_m was the physiological parameters of the

patient and the structural parameters of the coronary arteries. The patient's physiological parameters mainly included the heart rate (HR), systolic blood pressure (SP), diastolic blood pressure (DP), left ventricular end-systolic volume (ESV) and left ventricular end-diastolic volume (EDV), which could be retrieved from the Hospital Information System (HIS). As for the structural information of the coronary artery, it included the length of the blood vessel (L_v) and its cross-sectional area of the blood vessel (A_v), which were measured from the coronary artery reconstructed based on the patient's CTA images.

The reconstruction of the three-dimensional (3D) model was based on the patient's computed tomography image (CT). In this study, all coronary CTA examinations were performed on CT scanners with ≥ 64 detector rows (Revolution, GE, USA) and double cylinder high-pressure syringe (STELLANT, MEDRAD Inc., USA). The CT images in DICOM format were imported into Mimics Version 19.0 (Materialise, Inc., Belgium) software. Two professional technicians manually reconstructed the coronary artery tree and performed cross-checking. Coronary angiography was used as a control, and coronary vessels with a diameter of more than 1 mm were preserved. If the reconstructed model was different, then a third professional technician would perform the reconstruction. Finally, physicians with more than 10 years of clinical experience were invited to check all reconstructed 3D models to ensure the accuracy of the models.
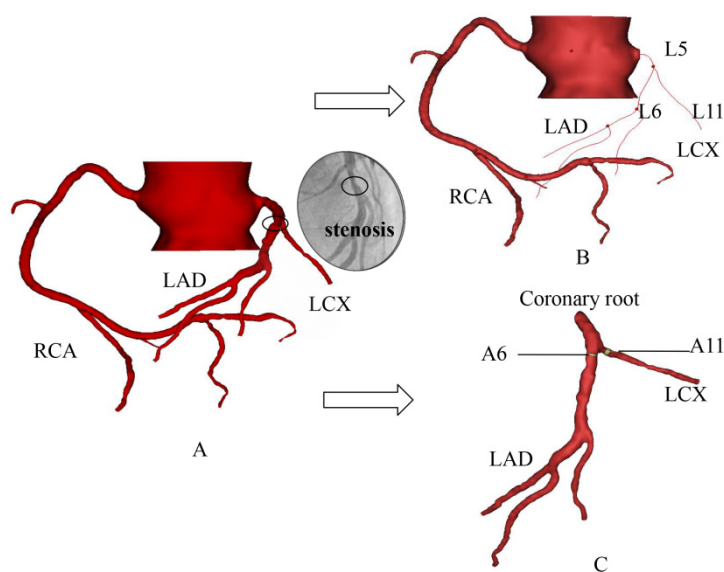

Figure 3. Coronary artery 3D reconstruction. (A) 3D reconstruction based on the patient's CT images. The stenosis was located in the left anterior descending branch (LAD), and vessels with a diameter of 1 mm or more were preserved. (B) The length from the root of the coronary artery to the first bifurcation was denoted as L5, the length from the first bifurcation to the second bifurcation was denoted as L6 on LAD, and the length from the first bifurcation node to the end of the blood vessel was denoted as L11 on the left circumflex (LCX). (C) After the first bifurcation, we measured the cross-sectional area of the blood vessel perpendicular to the center line, avoiding the stenosis, and marked the areas as A6 on the LAD and A11 on the LCX.

Each bifurcation of a blood vessel was represented as a node, and the distance between every

two nodes was defined as the length of the vessel. The centerline measurement method was more accurate, which could avoid the error caused by the blood vessel surface measurement. The size of the cross-sectional area was the size of the area where the diameter of the blood vessel did not drastically change after each node. It was necessary to ensure that the cross-section was perpendicular to the centerline of the blood vessel as much as possible [27,28], as shown in Figure 3.

The numerical calculation of R_m was carried out in an ideal state, i.e., the blood vessel was not narrowed. Based on the pressure drop and the mean blood vessel flow, the equivalent resistance for each coronary artery tree could be calculated, as shown in Eq (11). However, the pressure drop and flow could not be directly obtained in the real coronary artery model, and the calculation needed to be started from the coronary artery root.

Taken the model in Figure 4A as an example, the stenosis was located in the proximal part of LAD, and the resistance of the arterioles and capillaries after the bifurcation of the blood vessel was R_{6m}. The entire left coronary artery could be simplified as shown in Figure 4B. According to the principle of blood vessel modeling, the bifurcated blood vessel was equivalent to a parallel circuit [29], as shown in Figure 4C.
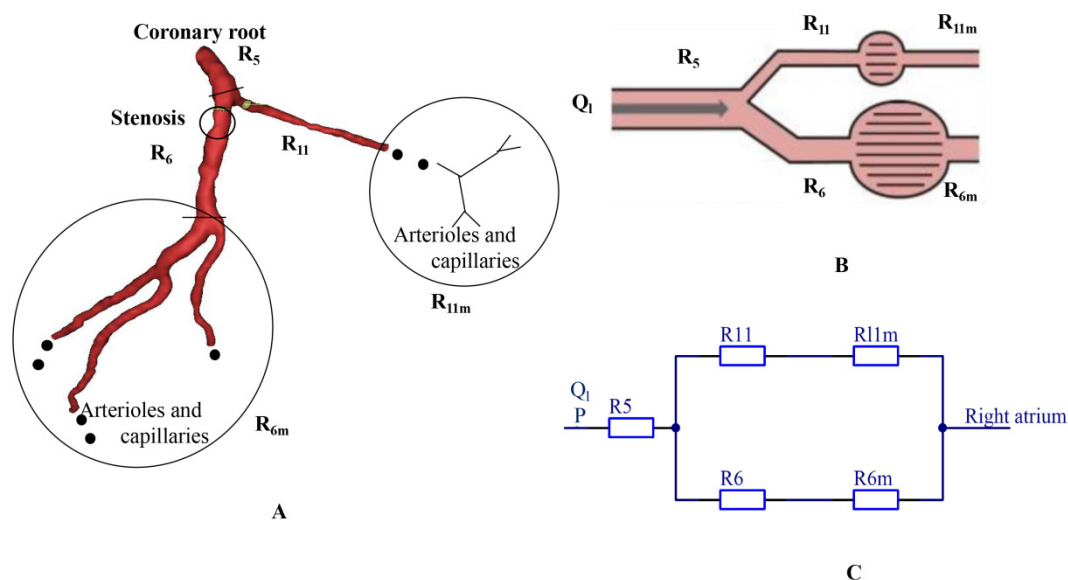

Figure 4. Rm calculation model. (A) There was a large number of small arteries and capillaries in the posterior segment of the blood vessel, which represented the main part of the Rm; (B) The simplified model of the left coronary artery. The resistance of each segment of the blood vessel was recorded as R5, R6 and R11. R6m and R11m represented the Rm at the back end of the blood vessel; (C) The resistance on the same blood vessel was a series circuit, and the bifurcated blood vessel was a parallel circuit.

In this process, the pressure of the right atrium was assumed to be 0 mmHg. The cardiac output Q_{co} could be obtained through ultrasonic measurement of EDV and ESV, assuming that the coronary flow Q_{cor} was 4% of the cardiac output, and the left coronary flow Q_l represented 60% of coronary flow [2,9,10,30]. The pressure P of the coronary artery was the mean arterial pressure, as shown in the Eqs (1)–(4).

$$Q_{co} = (EDV - ESV) * HR \tag{1}$$

$$Q_{cor} = Q_{co} * 4\% \tag{2}$$

$$Q_l = 60\% Q_{cor} \tag{3}$$

$$P = (SP + 2DP)/3 \tag{4}$$

The resistance of normal blood vessels was mainly caused by the blood viscosity. Coronary vessels were divided according to the bifurcation nodes, and the resistance of the vessels between each two nodes, such as R_5, R_6 and R_{11}, could be calculated according to Eq (5).

$$R_v = \frac{8\pi\eta L_V}{A_V^2} \tag{5}$$

where L_v denoted the length of the blood vessels of two branch nodes, Av was the cross-sectional area at the beginning of the vessel, and η represented a blood viscosity 0.0035 Pa·s.

The blood flow was proportional to the power of the diameter, and the flow of bifurcated blood vessels was obtained by Eq (6), in which i represented the number of forked nodes, i.e., the number of forked layers (i = 1, 2, 3...), and j represented the number of bifurcated vessels on a bifurcation node (j = 1, 2, 3...). In this study, the Rm values when α was 3, 2.7 and 7/3 were calculated and recorded as $3R_m$, $2.7R_m$ and $7/3R_m$, respectively.

$$Q_{ij} = \frac{D_{ij}^{\alpha}}{D_{i1}^{\alpha} + D_{i2}^{\alpha} \cdots + D_{ij}^{\alpha}} Q_l \tag{6}$$

By subtracting the pressure drop of the blood vessel from that of the coronary artery root, the pressure of the coronary microcirculation could be obtained in LAD. R_m was calculated by Eq (7).

$$R_m = \frac{p - \Delta p_1 - \Delta p_2 \cdots - \Delta p_i}{0.024 Q_{co}} * \left(\frac{D_{11}^{\alpha} + D_{12}^{\alpha} \cdots + D_{1j}^{\alpha}}{D_{1j}^{\alpha}} \cdot \frac{D_{21}^{\alpha} + D_{22}^{\alpha} \cdots + D_{2j}^{\alpha}}{D_{2j}^{\alpha}} \cdots \frac{D_{i1}^{\alpha} + D_{i2}^{\alpha} \cdots + D_{ij}^{\alpha}}{D_{ij}^{\alpha}} \right) \tag{7}$$

2.3. Simulation calculation under different power-law scaling

A widely recognized open-loop 0-3D geometric multi-scale model was used for FFRCT simulation calculation, as shown in Figure 5.
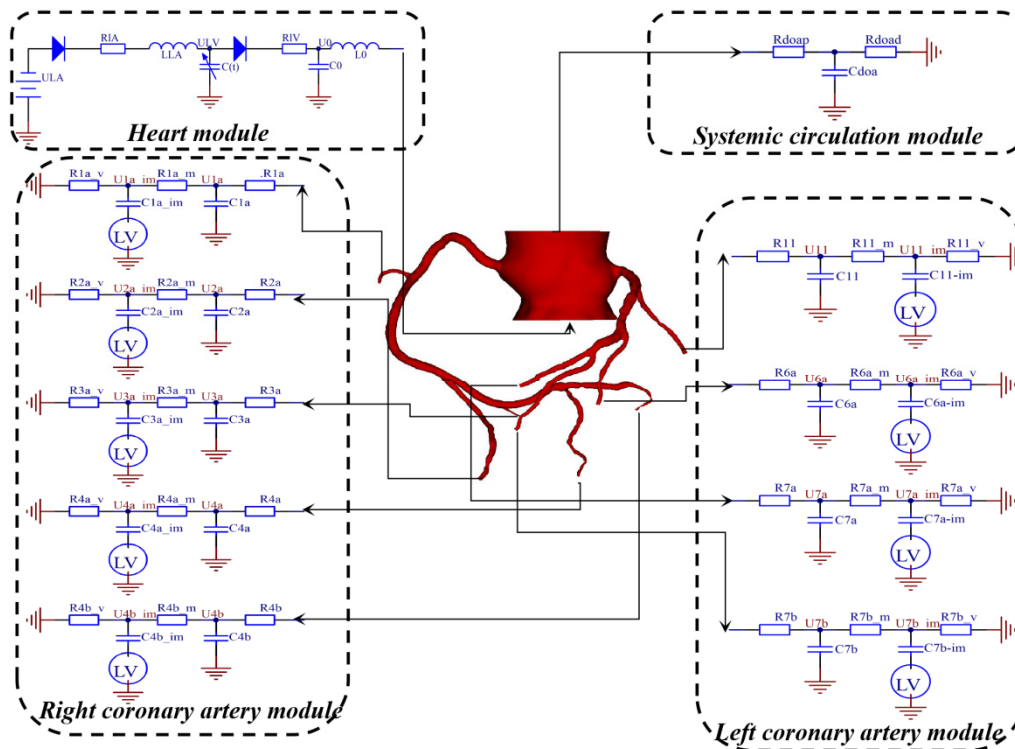
Figure 5. Open-loop 0-3D geometric multi-scale coupling model.

2.3.1. 3D model settings

In this study, all models were meshed using the tetrahedral meshing method in the ANSYS workbench 14.5 software. The simulation parameters were set in the ANSYS CFX 14.5 software. The material properties of blood were set as adiabatic, isotropic, incompressible Newtonian fluid with a density of 1050 kg/m3 and a viscosity of 0.0035 Pa·s. The blood vessel wall was defined as a non-slip rigid wall.

2.3.2. 0D model settings

In the geometric multi-scale model, the zero-dimensional (0D) part (lumped parameter model) was mainly composed of three modules: the heart module (inlet boundary conditions), systemic circulation module (systemic circulation exit boundary conditions) and coronary artery module (coronary exit boundary conditions). In each of these modules, the resistance (R) was used to simulate the flow resistance, the capacitance (C) was used to simulate the vascular compliance, and the inductance (L) was used to simulate the blood inertia. In the heart module, the heart valve was simulated by the diode, and the left ventricle was simulated by the variable capacitance C(t). At the same time, a left ventricular module (L$_V$) was added at the distal end of the coronary module to simulate the effect of myocardial contraction on the coronary blood flow.

The pressure-volume relationship was used in the ventricular module to describe the change in the variable capacitance in a cardiac cycle [27,31], as shown in Eq (8).

$$E(t) = \frac{P(t)}{V(t) - V_0} \tag{8}$$

where E(t) denoted the time-varying elasticity (mmHg/ml), which was the reciprocal of the variable capacitance C, V(t) and P(t) represented the time-varying ventricular volume (ml) and pressure (mmHg), respectively, and V0 (ml) denoted the reference solvent. Mathematically, Eq (9) was used to describe E(t):

$$E(t) = (E_{max} - E_{min}) \cdot E_n(t_n) + E_{min} \tag{9}$$

$E_n(t_n)$ represented the normalized time-varying elasticity, expressed in Eq (10):

$$E_n(t_n) = 1.55 \left[\frac{\left(\frac{t_n}{0.7}\right)^{1.9}}{1 + \left(\frac{t_n}{0.7}\right)^{1.9}} \right] \left[\frac{1}{1 + \left(\frac{t_n}{1.17}\right)^{21.9}} \right] \tag{10}$$

where $t_n = \frac{t}{T_{max}}$, $T_{max} = 0.1 + 0.15 t_c$, and t_c denoted the cardiac cycle (s).

In the coronary artery module, the coronary exit boundary conditions were Rm, mainly consisting of the coronary arterial resistance Ra, coronary arterial microcirculation resistance Ra-m and coronary venous microcirculation resistance Ra-v. According to literature, their proportions were 0.32, 0.52 and 0.16, respectively. When the patient transitioned from a resting state to a hyperemic state, the Rm became 0.24 times that of the resting state [10,27].

2.3.3. Coupling model settings

The upstream and downstream blood vessels of the 3D model were represented by a lumped parameter model and solved by the displayed Euler method. The two models were connected by interface conditions (pressure and flow were continuous). To realize the 0D/3D coupling, the software development was performed. The secondary development system was a user-defined subroutine based on the FORTRAN language.

2.3.4. Multi-method simulation settings

In order to verify the influence of the power law scaling of the blood flow diameter on the simulation results, we repeated the FFRCT simulation with 3Rm, 2.7Rm and 7/3Rm as the exit boundary conditions without changing any other settings, the simulation program or FFRCT measurement position. The results were recorded as 3FFRCT, 2.7FFRCT and 7/3FFRCT, respectively.

2.4. Statistical analysis

Statistical analysis was performed using the SPSS Version 23.0 (IBM, New York, USA) and MedCalc Version 15 (MedCalc Software, Ostend, Belgium) software. In the demographic analysis, continuous data were represented by the mean ± standard deviation and the correlation between continuous variables and FFR was expressed by ANOVA. Qualitative data were represented by the statistical frequency and percentage, and the chi-square test was used to express the correlation between qualitative variables and FFR. In the correlation analysis, a p-value of less than 0.05

indicated statistical significance.

The simulated FFRCT and the clinically measured FFR were continuous values, and the Bland-Altman diagram was chosen to analyze the consistency of the two methods. If the difference between the two measurement results was clinically acceptable, within the 95% limits of agreement (95% LoA), then a good agreement could be considered between the measurement results of the two methods. The smaller the 95% LoA, the better the consistency. The area under the curve (AUC) value of the receiver operating characteristic (ROC) was used as the criterion to evaluate the diagnostic performance. The closer the AUC to 1, the better the diagnostic performance.

3. Results

3.1. Patient characteristics

As shown in Table 1, there was a clear correlation between the Rm calculated under the three powers and the clinically measured FFR value. The average values of 3Rm, 2.7Rm and 7/3Rm were 146.02 ± 80.73, 149.13 ± 80.94 and 154.17 ± 83.59 mmHg/ml/s, and their p-values were 0.004, 0.005 and 0.010, respectively. Subsequently, the p-values of the correlation between gender, age, HR, SP, DP, EDV, ESV and invasive FFR were all greater than 0.05, indicating that the correlation was statistically insignificant.

Table 1. Patient characteristics.

Variables	Value	P value
Gender (male/female, percentage)	20/6, 76.9%	0.455
Age ($\bar{x} \pm S$, year)	60.73 ± 8.79	0.573
Heart rate ($\bar{x} \pm S$, beat/min)	66.86 ± 13.43	0.285
Systolic blood pressure ($\bar{x} \pm S$,mmHg)	127.57 ± 25.64	0.275
Diastolic blood pressure ($\bar{x} \pm S$,mmHg)	73.67 ± 16.24	0.293
Left ventricular end-systolic volume (ESV) ($\bar{x} \pm S$,ml/min)	81.79 ± 50.96	0.449
Left ventricular end-diastolic volume (EDV) ($\bar{x} \pm S$,ml/min)	60.45 ± 43.72	0.895
Calculated Rm under $Q \propto D^3$ (3Rm) ($\bar{x} \pm S$,mmHg/ml/s)	146.02 ± 80.73	0.004
Calculated Rm under $Q \propto D^{2.7}$ (2.7Rm) ($\bar{x} \pm S$,mmHg/ml/s)	149.13 ± 80.94	0.005
Calculated Rm under $Q \propto D^{7/3}$ (7/3Rm) ($\bar{x} \pm S$,mmHg/ml/s)	154.17 ± 83.60	0.010

3.2. Clinical reliability of the 3FFRCT, 2.7FFRCT and 7/3FFRCT

The average values of 3FFRCT, 2.7FFRCT and 7/3FFRCT were 0.827 ± 0.172, 0.825 ± 0.169 and 0.824 ± 0.167, respectively, which were slightly higher than the clinically measured FFR (0.814 ± 0.151). Figure 6 shows the scatter plot of FFRCT and FFR under the three different power-laws. The Pearson correlation coefficients of 3FFRCT, 2.7FFRCT and 7/3FFRCT with FFR were 0.95, 0.95 and 0.96, respectively, p-value < 0.001, indicating a good correlation between the results of the simulation calculation and those of the clinical measurement. In particular, the simulated 7/3FFRCT
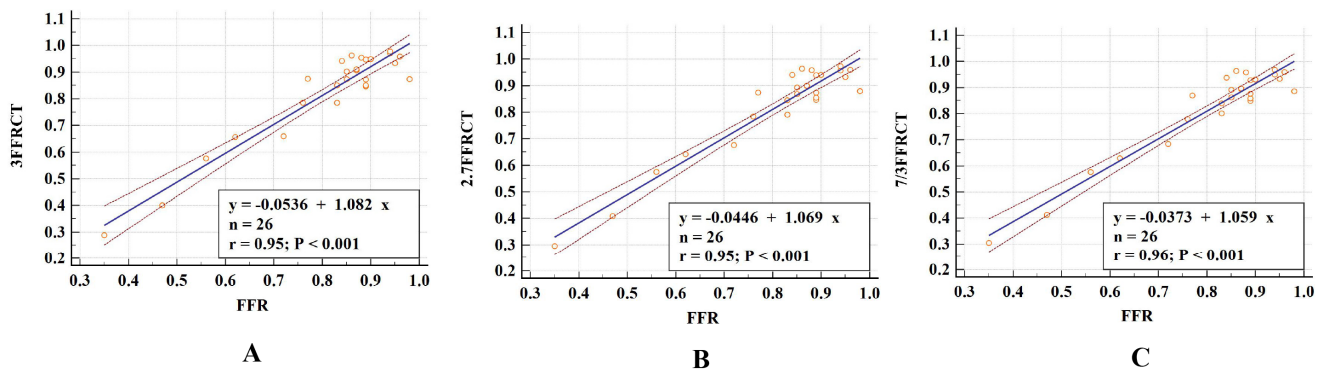
was slightly better than the other two.

Figure 6. Scatter plots of three kinds of blood flow-diameter.

Figure 7 shows the Bland-Altman diagram. The average difference between 3FFRCT, 2.7FFRCT, 7/3FFRCT and FFR was 0.01, and the 95% LoA were -0.11~0.12, -0.09~0.11 and -0.08~0.11 (n = 26), respectively. Obviously, FFRCT was slightly overestimated compared with the clinically measured FFR, but the results of 7/3FFRCT-FFRCT were most concentrated in the simulation results of the three different blood flow-diameter power laws.
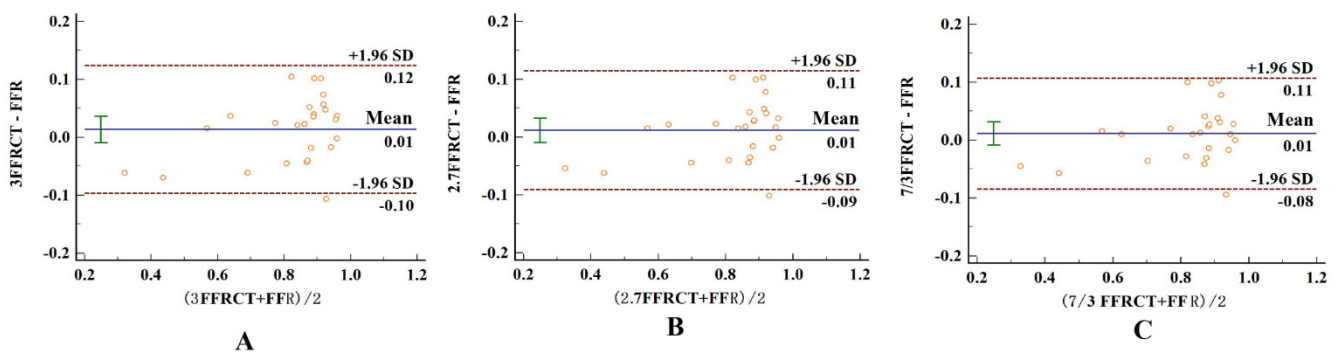

Figure 7. Bland-Altman diagram between three kinds of blood flow-diameter power-law simulation FFRCT and clinically measured FFR.

3.3. Diagnostic performance of FFRCT under three power-laws of blood flow-diameter

The diagnostic performance of FFRCT was evaluated using the ROC curve analysis. Figure 8 shows the ROC curve of FFRCT using a cut-off clinically measured FFR of ≤ 0.80. In the case of 3FFRCT, 2.7FFRCT and 7/3FFRCT, the AUC values were 0.944 [95% (CI): 0.777–0.996], 0.962 [95% (CI): 0.805–0.999], and 0.962 [95% (CI): 0.805–0.999], respectively.
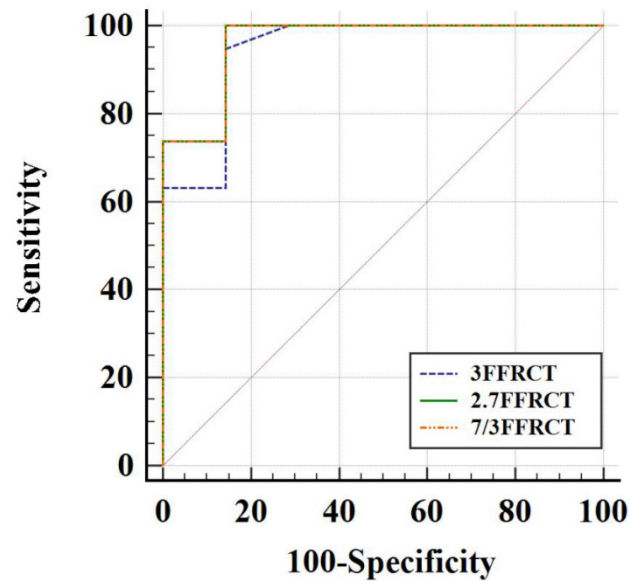
Figure 8. Receiver-operating characteristic (ROC) curve of FFRCT using the cut-off invasive FFR of ≤ 0.8 on a per-vessel basis. (A) The blue line represents the ROC curve of 3FFRCT; (B) The green line represents the ROC curve of 2.7FFRCT; (C) The orange line represents the ROC curve of 7/3FFRCT.

Correspondingly, the standard errors were 0.0536, 0.0400 and 0.0400, respectively, as shown in Table 2. The metrics of sensitivity, specificity, positive predictive value (NPV), negative predictive value (NPV) and accuracy were also important indicators for evaluating the diagnostic performance, as shown in Table 2.

Table 2. The diagnostic metrics of three numerical simulation results.

Diagnostic metrics	3FFRCT	2.7FFRCT	7/3FFRCT
AUC (95% CI)	0.944 (0.777–0.996)	0.962 (0.805–0.999)	0.962 (0.805–0.999)
SE	0.0536	0.0400	0.0400
Sensitivity	94.7%	100%	100%
Specificity	85.7%	85.7%	85.7%
PPV	85.7%	85.7%	85.7%
NPV	94.7%	100%	100%
Accuracy	92.3%	96.15%	96.15%
Threshold	0.816	0.787	0.791

2.7FFRCT and 7/3FFRCT had the same sensitivity, specificity, PPV, NPV and accuracy in judging myocardial ischemia, which were higher than the metrics of 3FFRCT. During the whole calculation process, the corresponding thresholds for judging the myocardial ischemia were 0.816,

0.787 and 0.791, respectively. The diagnostic threshold of 7/3FFRCT was the closest to 0.8. Based on the above-presented data, it was found that FFRCT had the best diagnostic performance when the blood flow-diameter power-law scaling was 7/3.

4. Discussion

The blood flow diameter power-law scaling combined the structure and function and represented the supply-demand relationship between blood and the myocardium. The variable power-law size affected the distribution of blood flow in the blood vessel. In addition, it further affected the setting of the CFD exit boundary condition Rm, which had special significance for the accuracy of the simulation results.

4.1. The relationship between Rm and FFR

A significant correlation between R_m and the clinically measured FFR can be observed in Table 1, which was closely related to the calculation method and process of Rm. The calculation method was explained by the theoretical simplified model, as shown in Figure 9.
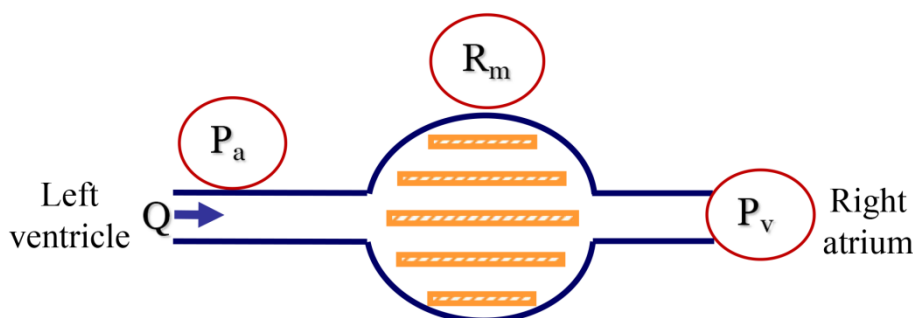

Figure 9. A simplified model explaining the calculation method.

Blood flow from the left ventricle into the blood vessel, and finally circulates to the right atrium through the capillaries. Since the pressure (P_v) of the right atrium is smaller than the pressure (Pa) of the left ventricle, this work assumed Pv to be 0 mmHg. Vascular resistance (R_v) is mainly caused by the blood viscosity, and the blood pressure drop (Δp) can be obtained. Then, the calculation method of Rm can be obtained by Ohm's law, as shown in Eq (11).

$$R_m = \frac{P_a - \Delta p}{Q} \tag{11}$$

Rm represented the resistance produced by all blood vessels at the back of the stenosis. In Equation 11, Δp denoted the pressure drop of a blood vessel, which is related to the length and cross-sectional area of the corresponding blood vessel. Similarly, Q represented the mean flow, which is affected by the diameter of the blood vessel. Throughout the entire calculation process, R_m did not only involve the patient's personalized physiological parameters, but also involved the patient's coronary artery structure. Therefore, the calculated R_m represented the predictive value of

the comprehensive calculation of the patient's structure and function evaluation.

4.2. Analysis of three kinds of simulation results and evaluation of diagnostic performance

The prediction threshold of 3FFRCT (0.816) was greater than 0.8, but the prediction threshold of 2.7FFRCT (0.787) and 7/3FFRCT (0.791) was less than 0.8. This was related to the data distribution. ROC curve analysis could get the Yoden index, as shown in the Eq (12).

$$\text{Youden Index} = \text{Sensitivity} + \text{Specificity} -1 \tag{12}$$

The value corresponding to the largest Youden index was the prediction threshold. In other words, the threshold was the value with the best sensitivity and specificity. The predicted threshold value distinguishes the result of ischemia and ischemia to the greatest extent consistent with the result of FFR judgment. According to the distribution of the simulation results, the ROC curve analysis automatically calculated the points with the highest sensitivity and specificity to obtain the predicted threshold. The distribution of FFRCT data was not the same, and the prediction threshold was also different. However, the closer the threshold was to 0.8, the closer the distribution of FFRCT was to that of FFR.

Figure 7 shows that the average difference between 2.7FFRCT, 7/3FFRCT and clinical FFR was 0.01, which showed that the simulation results overestimated FFR. Correspondingly, Table 2 shows that the prediction threshold of 2.7FFRCT and 7/3FFRCT was lower than 0.8. This phenomenon was related to the data processing method. FFR was a continuous variable when performing Bland-Altman diagram analysis. In contrast, the thresholds of the three methods were predicted by ROC curve analysis, with FFRCT as the test variable and FFR (0.8) as the state variable. FFR was a categorical variable. FFR ≥ 0.8 was defined as non-ischemic, and FFR < 0.8 was defined as ischemic. So, for non-ischemic data, no matter whether FFRCT was 0.8 or 1, there was almost no difference for the ROC curve.

4.3. Effect of the three kinds of blood flow-diameter power-law scaling on the flow in bifurcated vessels

The allometric scaling law represents the basis to understand the morphological and hemodynamic characteristics of biological vascular trees and is of great significance to the construction of vascular models. In this work, we found that having blood flow proportional to the power 7/3 of the diameter is more suitable for the simulation calculation of FFRCT, and it has a higher accuracy than the FFRCT calculated by the powers 3 and 2.7. This phenomenon may be related to the geometry of the coronary artery.

The influence of the coronary artery structure on the blood flow diameter scaling law was mainly reflected in the branch diameters of blood vessels of the same bifurcated vessel. Assuming that the stenosis was on vessel j of branch i, and there were two vessels at the bifurcation, the blood flow of the vessel could be calculated as in Eq (6). $D_{ij}/D_{i(j+1)}$ could represent the relative size of the blood vessel in which the stenosis was located, represented by the letter A. Then the formula can be transformed into Eq (13).

$$Q_{ij} = (1 - \frac{1}{A^{\alpha}+1}) \ Q_l \tag{13}$$

This is a piecewise function. When A was greater than 1, as the power increased, the flow gradually increased, and A when was less than 1, as the power increased, the flow gradually decreased. Correspondingly, only when A was 1, no matter how the power changed, it would not affect the flow. This phenomenon leads to a greater dispersion of FFRCT obtained by simulation when the power is 3. In the past 80 years, many papers on Murray's law and exponential verification have been published. These studies show that the 3.0 application has significant dispersibility in all coronary trees with an internal flow that obeys laminar flow conditions [14–20]. This may be the reason why 7/3FFRCT is better than the other two methods.

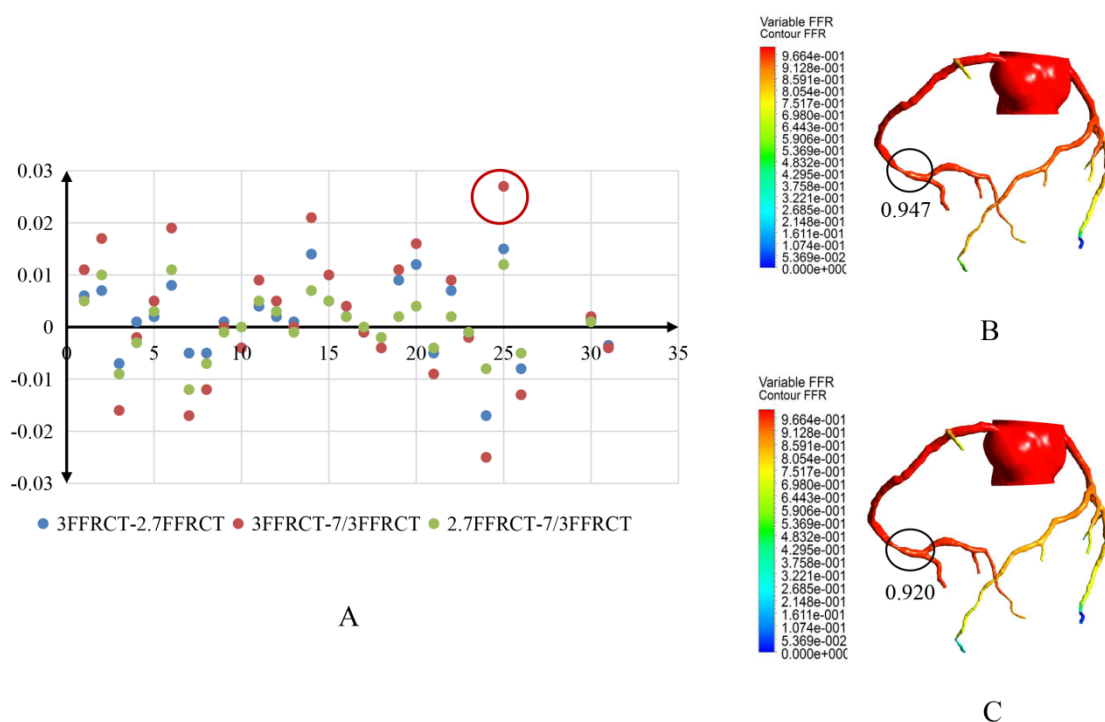*4.4. The differences among three kinds of results*

Figure 10. Scatter plot of the differences between the three types of FFRCT. The figure shows the differences in three kinds of simulation results of 26 patients. The blue dots represent the difference between 3FFRCT and 2.7FFRCT; the red dots represent the difference between 3FFRCT and 7/3FFRCT; and the green dots represent the difference between 2.7FFRCT and 7/3FFRCT. The simulation result of the 25th patient has the largest difference, which is 0.027 marked with a red circle. The FFR cloud chart of patients with the largest results difference under the three kinds of blood flow-diameter scaling laws.

The simulation results of the three power scaling laws did not show much change, but this phenomenon was acceptable. The scatter plots of the difference between 3FFRCT and 2.7FFRCT, 3FFRCT and 7/3FFRCT, and 2.7FFRCT and 7/3FFRCT were shown in Figure 10A. It could be found that the maximum difference of the simulation results was 0.027, and its corresponding 3FFRCT and 7/3FFRCT values were 0.947 and 0.920, respectively, as shown in Figure 10B and 10C. Correspondingly, the difference between $3R_m$ and $7/3R_m$ was 84 mmHg/ml/s. Previous works that the

R_m in the hyperemic state to be 0.24 times R_m in the resting state [29], which narrows the gap in the exit boundary conditions simulated by FFRCT. At the same time, FFR is a dimensionless value between 0–1 [8,29,31], which further narrows the gap between the simulation results of different power scaling laws.

4.5. Application of blood flow diameter scaling law in recent research methods

The simulation of FFRCT makes non-invasive FFR calculation possible, which has passed the FDA certification [1,6]. However, it has disadvantages, including the long time of the entire process, large amount of calculation and complicated operation. This makes non-professionals unable to operate it, so the simulation results cannot be presented in real time and the clinical development of this technology is limited.

The rapid development of machine learning (ML) has made the application of FFRCT possible. The process of using ML generally consists of four parts: 1) the ML framework is built; 2) the training set is used for supervised learning; 3) the verification set is used to determine the parameters of the network; 4) the test set is used to verify the optimal performance of the model. Previous research focused on the ML framework, such as random forest (RF), self-organizing map (SOM), support vector machine (SVM), fully connected neural network (FC), long and short-term memory unit (LSTM), TreeVes -D, TreeVes-U and TreeVes-Net [32–36].

However, the training set includes a set of samples of known categories to adjust the parameters of the classifier to achieve the required performance. Hence, the accuracy of the training set is very important. The method of this research improves the accuracy of FFRCT, which can be applied to improve the accuracy of the training set and validation set. This lays the foundation for the use of machine learning in the flow field in the coronary arteries.

smartFFR was a new method of true onsite and real-time, geometrically derived coronary artery stenosis function assessment. Its inlet boundary condition was an average static pressure of 100 mmHg, and its outlet boundary condition was an increased transient flow profile. In order to do this, after evaluating the diameter and cross-sectional area of the branch, Murray's law was applied, which stated that the flow of the branch was proportional to 3 exponent of the corresponding diameter of the branch. This study pointed out that the accuracy of FFRCT simulation with an application of the 7/3 exponent was higher than that of the 3 exponent. In future work, it could be applied to smartFFR to check whether 7/3 could improve the accuracy of smartFFR [37].

4.6. Limitations

This work had some limitations. Firstly, the number of enrolled groups was not large enough, the selection of data was biased, and there were fewer ischemic vessels than non-ischemic vessels. Secondly, the research performed based on the assumption that the ratio of flow distribution between the left and right coronary arteries was 6:4, which was not personalized. Finally, a constant blood viscosity value of 0.0035 Pa.s was applied in the simulation, which was not a personalized value.

5. Conclusions

The blood flow-diameter power-law scaling affects the calculation of blood flow distribution

and microcirculation resistance; hence, it affects the simulation results of FFRCT. This paper simulated and calculated FFRCT in the case of 3, 2.7 and 7/3 powers. Through retrospective analysis between these results and invasive FFR, the accuracy of FFRCT was shown to be the highest when the blood flow diameter scale law was 7/3. This has positive significance for the improvement of the FFRCT model and the accuracy of the model.

Acknowledgement

Ethics approval and participant consent

This study passed the inspection by the medical ethics committee of Peking University People's Hospital. All participants have signed an informed consent.

Conflict of interest

The authors declare that there is no conflict of interests of this article.

References

1. N. H. J. Pijls, B. DeBruyne, K. Peels, P. H. VanderVoort, H. Bonnier, J. Bartunek, et al., Measurement of fractional flow reserve to assess the functional severity of coronary-artery stenoses, *N. Engl. J. Med.*, **334** (1996), 1703–1708. https://doi.org/10.1056/NEJM199606273342604

2. Y. Feng, B. Y. Mao, B. Li, J. Liu, J. C. Liu, Y. J. Liu, Effect of hemodynamic parameters on fractional flow reserve, *J. Mech. Med. Biol.*, **20** (2020), 14. https://doi.org/10.1142/S0219519420500177

3. N. Kakouros, F. J. Rybicki, D. Mitsouras, J. M. Miller, Coronary pressure-derived fractional flow reserve in the assessment of coronary artery stenoses, *Eur. Radiol.*, **23** (2013), 958–967. https://doi.org/10.1007/s00330-012-2670-4

4. C. Ball, G. Pontone, M. Rabbat, Fractional flow reserve derived from coronary computed tomography angiography datasets: The next frontier in noninvasive assessment of coronary artery disease, *Biomed. Res. Int.*, (2018), 8. https://doi.org/10.1155/2018/2680430

5. S. X. Tu, J. Westra, J. Adjedj, D. X. Ding, F. Y. Liang, B. Xu, et al., Fractional flow reserve in clinical practice: from wire-based invasive measurement to image-based computation, *Eur. Heart J.*, **41** (2020), 3271–3279. https://doi.org/10.1093/eurheartj/ehz918

6. M. T. Lu, M. Ferencik, R. S. Roberts, K. L. Lee, A. Ivanov, E. Adami, et al., Noninvasive FFR derived from coronary CT angiography management and outcomes in the PROMISE trial, *JACC Cardiovasc. Imaging*, **10** (2017), 1350–1358. https://doi.org/10.1016/j.jcmg.2016.11.024

7. B. K. Koo, A. Erglis, J. H. Doh, D. V. Daniels, S. Jegere, H. S. Kim, et al., Diagnosis of ischemia-causing coronary stenoses by noninvasive fractional flow reserve computed from coronary computed tomographic angiograms. Results from the prospective multicenter DISCOVER-FLOW (Diagnosis of Ischemia-Causing Stenoses Obtained Via Noninvasive Fractional Flow Reserve) Study, *J. Am. Coll. Cardiol.*, **58** (2011), 1989–1997. https://doi.org/10.1016/j.jacc.2011.06.066

8. J. K. Min, D. S. Berman, M. J. Budoff, F. A. Jaffer, J. Leipsic, M. B. Leon, et al., Rationale and design of the DeFACTO (Determination of Fractional Flow Reserve by Anatomic Computed Tomographic AngiOgraphy) study, *J. Cardiovasc. Comput. Tomogr.*, **5** (2011), 301–309.

9. C. A. Taylor, T. A. Fonte, J. K. Min, Computational fluid dynamics applied to cardiac computed tomography for noninvasive quantification of fractional flow reserve scientific basis, *JACC*, **61** (2013), 2233–2241. https://doi.org/10.1016/j.jacc.2012.11.083

10. H. J. Kim, I. E. Vignon-Clementel, J. S. Coogan, C. A. Figueroa, K. E. Jansen, C. A. Taylor, Patient-specific modeling of blood flow and pressure in human coronary arteries, *Ann. Biomed. Eng.*, **38** (2010), 3195–3209. https://doi.org/10.1007/s10439-010-0083-6

11. C. K. Zarins, C. A. Taylor, J. K. Min, Computed fractional flow reserve (FFTCT) derived from coronary CT angiography, *J. Cardiovasc. Transl. Res.*, **6** (2013), 708–714. https://doi.org/10.1007/s12265-013-9498-4

12. M. Gotberg, E. H. Christiansen, I. J. Gudmundsdottir, L. Sandhall, M. Danielewicz, L. Jakobsen, et al., Instantaneous wave-free ratio versus fractional flow reserve to guide PCI, *N. Engl. J. Med.*, **376** (2017), 1813–1823. https://doi.org/10.1056/NEJMoa1616540

13. Y. P. van de Hoef, F. Nolte, P. Damman, R. Delewi, M. Bax, S. A. J. Chamuleau, et al., Diagnostic accuracy of combined intracoronary pressure and flow velocity information during baseline conditions adenosine-free assessment of functional coronary lesion severity, *Circ. Cardiovasc. Interv.*, **5** (2012), 508–514. https://doi.org/10.1161/CIRCINTERVENTIONS.111.965707

14. G. S. Kassab, J. Berkley, Y. C. B. Fung, Analysis of pig's coronary arterial blood flow with detailed anatomical data, *Ann. Biomed. Eng.*, **25** (1997), 204–217. https://doi.org/10.1007/BF02738551

15. G. S. Kassab, Y. C. B. Fung, The pattern of coronary arteriolar bifurcations and the uniform shear hypothesis, *Ann. Biomed. Eng.*, **23** (1995), 13–20. https://doi.org/10.1007/bf02368296

16. G. S. Kassab, C. A. Rider, N. J. Tang, Y. C. B. Fung, Morphometry of pig coronary arterial trees, *Am. J. Physiol.*, **265** (1993), 350–365. https://doi.org/10.1152/ajpheart.1993.265.1.H350

17. Y. L. Huo, G. S. Kassab, Intraspecific scaling laws of vascular trees, *J. R. Soc. Interface*, **9** (2012), 190–200. https://doi.org/10.1098/rsif.2011.0270

18. T. F. Sherman, On connecting large vessels to small-the meaning of murray law, *J. Gen. Physiol.*, **78** (1981), 431–453. https://doi.org/10.1085/jgp.78.4.431

19. Y. F. Zhou, G. S. Kassab, S. Molloi, On the design of the coronary arterial tree: a generalization of Murray's law, *Phys. Med. Biol.*, **44** (1999), 2929–2945. https://doi.org/10.1088/0031-9155/44/12/306

20. G. S. Kassab, Scaling laws of vascular trees: of form and function, *Am. J. Physiol. Heart Circ. Physiol.*, **290** (2006), H894–H903. https://doi.org/10.1152/ajpheart.00579.2005

21. L. Itu, P. Sharma, C. Suciu, F. Moldoveanu, D. Comaniciu, Personalized blood flow computations: A hierarchical parameter estimation framework for tuning boundary conditions, *Int. J. Numer. Method Biomed. Eng.*, **33** (2017), e02823. https://doi.org/10.1002/cnm.2803

22. J. P. H. M. van den Wijngaard, J. C. V. Schwarz, P. van Horssen, M. van Lier, J. G. G. Dobbe, J. A. E. Spaan, et al., 3D Imaging of vascular networks for biophysical modeling of perfusion distribution within the heart, *J. Biomech.*, **46** (2013), 229–239. https://doi.org/10.1016/j.jbiomech.2012.11.027

23. J. M. Zhang, T. Luo, S. Y. Tan, A. M. Lomarda, A. S. L. Wong, F. Y. J. Keng, et al., Hemodynamic analysis of patient-specific coronary artery tree, *Int. J. Numer. Method Biomed. Eng.*, **31** (2015), e02708. https://doi.org/10.1002/cnm.2708

24. M. Rabbat, J. Leipsic, J. Bax, B. Kauh, R. Verma, D. Doukas, et al., Fractional flow reserve derived from coronary computed tomography angiography safely defers invasive coronary angiography in patients with stable coronary artery disease, *J. Clin. Med.*, **9** (2020), 15. https://doi.org/10.3390/jcm9020604

25. J. K. Min, J. Leipsic, M. J. Pencina, D. S. Berman, B. K. Koo, C. van Mieghem, et al., Diagnostic accuracy of fractional flow reserve from anatomic CT angiography, *JAMA*, **308** (2012), 1237–1245. https://doi.org/10.1001/2012.jama.11274

26. A. Wahle, E. Wellnhofer, I. Mugaragu, H. U. Sauer, H. Oswald, E. Fleck, Quantitative volume analysis of coronary vessel systems by 3-D reconstruction from biplane angiograms, in *1993 IEEE Conference Record Nuclear Science Symposium and Medical Imaging Conference*, **3** (1993), 1217–1221. https://doi.org/10.1109/NSSMIC.1993.701838

27. B. Y. Mao, W. X. Wang, Z. Zhao, X. Zhao, L. L. Li, H. X. Zhang, et al., On the relationship between competitive flow and FFT analysis of the flow waves in the left internal mammary artery graft in the process of CABG, *Biomed. Eng. Online*, **15** (2016), 557–567. https://doi.org/10.1186/s12938-016-0260-4

28. G. B. West, J. H. Brown, B. J. Enquist, The fourth dimension of life: Fractal geometry and allometric scaling of organisms, *Science*, **284** (1999), 1677–1679. https://doi.org/10.1126/science.284.5420.1677

29. C. Tesche, K. Otani, C. N. de Cecco, A. Coenen, J. De Geer, M. Kruk, et al., Influence of coronary calcium on diagnostic performance of machine learning CT-FFR results from machine registry, *JACC Cardiovasc. Imaging*, **13** (2020), 760–770. https://doi.org/10.1016/j.jcmg.2019.06.027

30. J. K. Min, D. Berman, L. J. Shaw, L. Mauri, B. K. Koo, C. van Mieghem, et al., Fractional flow reserved derived from computed tomographic angiography (FFRCT) to discriminate individuals with versus without Ischemia: Results from the DeFACTO trial (determination of fractional flow reserve by anatomic computed tomographic angiography), *Circulation*, **126** (2012).

31. J. Escaned, M. Echavarria-Pinto, H. M. Garcia-Garcia, T. P. van de Hoef, T. de Vries, P. Kaul, et al., Prospective assessment of the diagnostic accuracy of instantaneous wave-free ratio to assess coronary stenosis relevance: results of ADVISE II International, Multicenter Study (ADenosine Vasodilator Independent Stenosis Evaluation II), *JACC Cardiovasc. Interv.*, **8** (2015), 824–833. https://doi.org/10.1016/j.jcin.2015.01.029

32. L. Itu, S. Rapaka, T. Passerini, B. Georgescu, C. Schwemmer, M. Schoebinger, et al., A machine-learning approach for computation of fractional flow reserve from coronary computed tomography, *J. Appl. Physiol.*, **121** (2015), 42–52. https://doi.org/10.1152/japplphysiol.00752.2015

33. K. Greff, R. K. Srivastava, J. Koutník, B. R. Steunebrink, J. Schmidhuber, LSTM: a search space odyssey, *IEEE Trans. Neural Networks Learn. Syst.*, **28** (2017), 2222–2232. https://doi.org/10.1109/TNNLS.2016.2582924

34. Z. Gao, Y. Li, Y. Sun, J. Yang, H. Xiong, H. Zhang, et al., Motion tracking of the carotid artery wall from ultrasound image sequences: a nonlinear state-space approach, *IEEE Trans. Med. Imaging*, **37** (2018), 273–283. https://doi.org/10.1109/TMI.2017.2746879

35. Z. Gao, X. Liu, S. Qi, W. Wu, W. K. Hau, H. Zhan, Automatic segmentation of coronary tree in CT angiography images, *Int. J. Adapt. Control Signal Process.*, **33** (2019), 1239–1247. https://doi.org/10.1002/acs.2762

36. Z. Gao, X. Wang, S. Sun, D. Wu, J. Bai, Y. Yin, et al., Learning physical properties in complex visual scenes: An intelligent machine for perceiving blood flow dynamics from static CT angiography imaging, *Neural Networks*, **123** (2020), 82–93. https://doi.org/10.1016/j.neunet.2019.11.017

37. P. K. Siogkas, L. Lakkas, A. I. Sakellarios, G. Rigas, S. Kyriakidis, K. A. Stefanou, et al., SmartFFR, a new functional index of coronary stenosis: comparison with invasive ffr data, *Front. Cardiovasc. Med.*, (2021), 958. https://doi.org/10.3389/fcvm.2021.714471